

Electronic Effect in a Ruthenium Catalyst Designed in Nanoporous N-Functionalized Carbon for Efficient Hydrogenation of Heteroarenes

Debraj Chandra,* Shikha Saini, Saswata Bhattacharya,* Asim Bhaumik, Keigo Kamata, and Michikazu Hara*



Cite This: <https://dx.doi.org/10.1021/acsami.0c15407>



Read Online

ACCESS |



Metrics & More



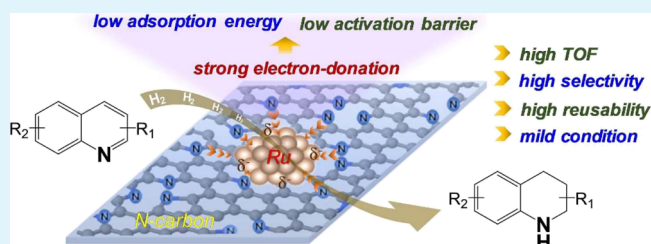
Article Recommendations



Supporting Information

ABSTRACT: Active metal catalysts are the key in chemical industry for sustainable production of multitude of chemical resources. Here, we report a new ruthenium (Ru) composite with a synergistically controlled nanostructure and electronic properties as a highly efficient hydrogenation catalyst which comprises stable small Ru nanoparticles (mean particle size, *ca.* 0.9 nm) in situ generated into a nanoporous N-functionalized carbon with high surface area (*ca.* 650 m² g⁻¹) and has strong electron-donating power of Ru sites of nanoparticles. The scalable and highly reusable catalyst, prepared from a self-assembled Ru complex, performs actively with low per metal usage under mild conditions (60–80 °C and 0.5–1.0 MPa H₂) for selective hydrogenation of various quinolines and pyridines. The role of electron-donating properties of the new Ru nano hybrid for highly efficient catalysis was characterized by both experiments and computational studies. Density functional theory calculations reveal that weak adsorption energies of quinoline at the electron-rich Ru surface prevents poisoning caused by its strong coordination and provides excellent reusability of the catalyst, while low activation barriers for the hydrogenation steps of the N-heterocyclic ring correlate with high catalytic activity. Our catalyst exhibits 5–24-fold higher turnover frequency up to *ca.* 167 h⁻¹ among the efficient noble metal catalysts reported for selective hydrogenation of quinoline to 1,2,3,4-tetrahydroquinoline.

KEYWORDS: ruthenium, nanostructure engineering, electronic property, catalyst, selective hydrogenation, heteroarenes, DFT



INTRODUCTION

Metal catalysts represent many state-of-the-art technologies for the production of important chemical resources.^{1–3} Among the various metal catalyst architectures, supported metal catalysts [*i.e.* metal nanoparticles (NPs) dispersed on heterogeneous supports] have been studied extensively.^{1,2,4–9} Their performance is often governed by the nature of metal–support interaction, which is strongly related to their structures.^{7,8} In this context, the long-standing concerns are downsizing the metal NPs for maximizing the atom utilization efficiency,^{5,6} controlling the shape of metal NPs to create more active surfaces,^{3,9,10} and designing functionalized supports, which strongly influence the local electronic structure of the materials.^{4,11} These parameters independently dictate the intrinsic activity and selectivity of many supported metal catalysts.^{5,6,9,11,12} However, tuning the size/shape of metal NPs and electronic structure of the material synergistically remain a significant challenge but crucial for the rational development of active metal catalysts.

Catalytic hydrogenation of heteroarenes is a fundamentally important reaction in many synthetic chemical processes.^{13–18} For instance, direct hydrogenation of quinoline derivatives is

immensely important for the selective production of 1,2,3,4-tetrahydroquinolines, a core structural motif in numerous pharmaceuticals, agrochemicals, and fine chemicals.^{19–21} To date, most of the practical heterogeneous systems for the direct hydrogenation of N-heteroarenes are mainly based on support catalysts of noble metals such as Pt,²² Pd,^{23–25} Rh,²⁶ Au,^{27,28} Ru,^{29–33} and Ir.⁶ Unfortunately, these noble metal catalysts are often hampered by lack of regioselectivity,³¹ low functional group tolerance,²⁴ and poor recyclability.³⁰ Particularly, in most cases, the catalysts are difficult to recycle because of deactivation/poisoning of the metal NPs by strong interaction with the heteroatoms.^{29,30,34} Moreover, high catalytic performance with low per metal is extremely desired at present scenario to improve the sustainability of sparse noble metal-based catalysts. The drawbacks of non-noble metal-based

Received: August 27, 2020

Accepted: November 3, 2020

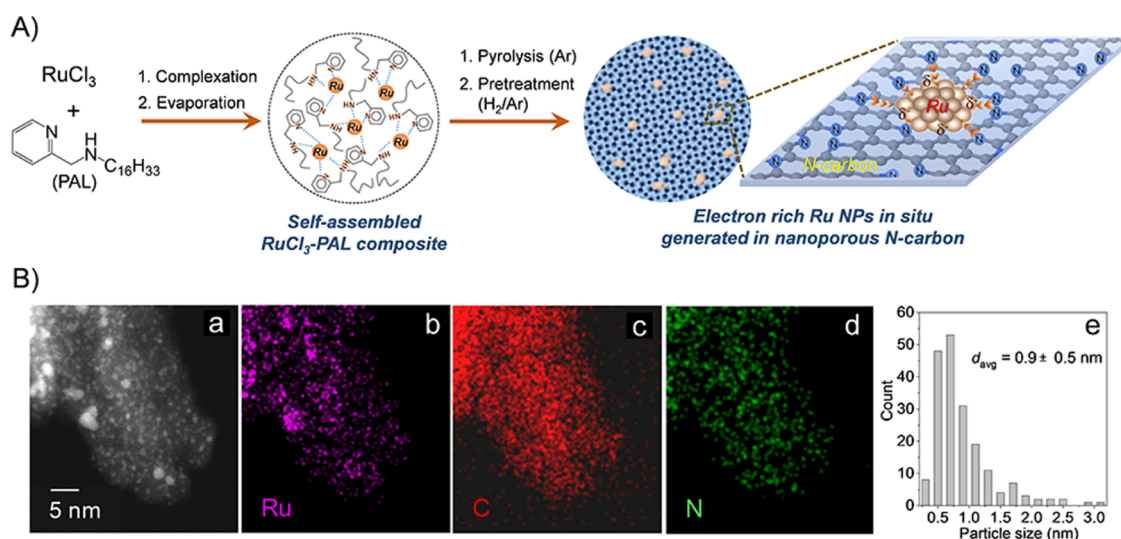


Figure 1. (A) Schematic illustration of the preparation of electron-rich small Ru NPs encapsulated in nanoporous N-carbon. (B) (a) HAADF-STEM image, (b–d) EDX elemental maps for Ru, C, and N, and (e) metal particle size distribution histogram of Ru-PAL-800 ($R_{\text{PAL}/\text{Ru}} = 12$) prepared at pH 1. Metal particle size distribution histogram was derived from Figure 1B(a).

catalysts are poor stability, requirement of harsh reaction condition (>120 °C and/or ≥ 2 MPa H₂), and long reaction times (mostly >24 h) due to their low capability for H₂ activation.^{21,35,36} These create an inevitable need for the chemical industry to design a robust and reusable metal catalyst for efficient hydrogenation of N-heteroarenes under mild conditions.

Nowadays, Ru-based nanomaterials are of pivotal importance in numerous catalytic applications (synthetic-organic processes,^{3,37} ammonia synthesis,^{4,38} Fischer–Tropsch reactions,³⁹ CO methanation/oxidation,^{10,40} water-splitting,⁴¹ and so forth). In the pursuit of a high-performance Ru catalyst for hydrogenation of N-heteroarenes, we have focused on the nitrogen-containing carbon (N-carbon) as a functionalized support, in which incorporated N-atoms can strongly affect the physicochemical and catalytic properties by the metal–support electronic interaction.^{42,43} Huge efforts have been devoted in recent years to the development of more active N-carbon modified metal-based materials including Ru ones.^{2,6,43–48} However, limited attention has been focused toward the control of electronic properties of metal sites in these materials. Electronic properties of metal sites can have a strong effect on the catalytic performance, even for the metal NPs of similar size.^{3,4,7} Herein, we report a newly developed Ru nanocomposite of N-carbon, having strong electron-donating properties of Ru, which is designed from a self-assembled Ru complex. The novel Ru nanocomposite catalyst provides (1) high atom-utility from stable sub-nanometer Ru NPs, in situ generated in N-carbon; (2) very high surface area of the nanoporous network; and (3) strong electron-donating effect of Ru sites in the small NPs, due to effective charge transfer with N-carbon. The Ru nanocomposite catalyst enables selective hydrogenation of several N-heteroarenes at markedly high reaction rates with low per metal usage and performs as a highly reusable catalyst. The role of electron-donating properties for the efficient catalytic performance is investigated by both experimental and computational studies.

RESULTS AND DISCUSSION

Preparation and Screening of the Catalysts. An organic amphiphilic molecule, 2-(hexadecylaminomethyl)pyridine (PAL),^{49,50} has been used as a structure-directing template as well as the source for carbon and nitrogen. The preparation is based on a simple two-step strategy (Figure 1A) involving complexation of the PAL (through N-sites) with RuCl₃ in ethanol/water, followed by slow evaporation of the solvent resulting in a self-assembled RuCl₃-PAL composite and then pyrolysis (600 °C, under Ar) of the RuCl₃-PAL composite and subsequent pretreatment (600–1000 °C, under H₂/Ar) of the carbonized product to produce the final material (see the Supporting Information). A series of catalysts (denoted as Ru-PAL- x ; x labels the pretreatment temperature) were prepared by varying the PAL/Ru molar ratio ($R_{\text{PAL}/\text{Ru}}$), synthesis pH, and pretreatment temperature (Table S1). The Ru contents are in the range of 4.9–5.5 and 10.3–12.2 wt % in the Ru-PAL- x catalysts prepared with $R_{\text{PAL}/\text{Ru}}$ of 12 and 6, respectively. The specific surface area, Ru dispersion, and particle size of Ru-PAL- x catalysts are summarized in Table S2.

Initial screening among the Ru-PAL- x catalysts was done based on the specific surface area and a preliminary catalytic test for an industrially important hydrogenation reaction of phenol to cyclohexanol.^{51,52} Ru-PAL- x prepared with $R_{\text{PAL}/\text{Ru}}$ of 12 gave overall better results than that with $R_{\text{PAL}/\text{Ru}}$ of 6 (Table S1 and Figure S1). Cyclohexanol yield (in 2 h) was increased by a factor of 3.4 (Table S1, entry 1–4; Figure S1B) with a decrease of the synthesis pH from 9 to 1 for Ru-PAL-600 ($R_{\text{PAL}/\text{Ru}} = 12$). Best catalytic performance was observed at 800 °C pretreatment for Ru-PAL-800 ($R_{\text{PAL}/\text{Ru}} = 12$) prepared at pH 1 (Table S1, entry 5–7; Figure S1D). X-ray photoelectron spectroscopic (XPS) analysis in Ru 3d and 3p regions (Figure S2) for the catalysts prepared at pH 1 shows peaks of Ru-PAL-600 (280.5 and 463.1 eV for Ru 3d_{5/2} and Ru 3p_{3/2}, respectively) shifted to lower binding energies in Ru-PAL-800 (279.9 and 462.2 eV for Ru 3d_{5/2} and Ru 3p_{3/2}, respectively), depicting that complete reduction of Ru³⁺ species to metallic Ru⁰ at 800 °C has improved the catalytic activity. However, incomplete reduction of Ru³⁺ species was observed for Ru-PAL-800 prepared at pH 9

perhaps due to its stronger binding with N-donor sites in basic pH.⁵⁴ Ru-PAL-*x* ($R_{\text{PAL/Ru}} = 12$; synthesis pH 1) was employed in the following experiments.

Detailed Characterization of the Structure of the Catalyst. Representative high-angle annular dark-field scanning transmission electron microscopy (HAADF-STEM) images of Ru-PAL-800 (Figures 1B(a) and S3) revealed the formation of finely dispersed and ultra-small Ru NPs except for few slightly larger particles. The particle size distribution (Figure 1B(e)) shows the presence of Ru NPs in the range of 0.4–3.1 nm, whereas the mean particle size was estimated to be in the sub-nanometer range of *ca.* 0.9 nm. However, the average particle size estimated from CO chemisorption was 1.9 nm for Ru-PAL-800 (Table S2), perhaps due to the input of the larger particles and/or restricted accessibility of CO molecules to some of the Ru NPs, encapsulated by carbon during high-temperature synthesis. The energy dispersive X-ray spectroscopy (EDX) maps (Figure 1B(b–d)) show that the N element is homogeneously dispersed in the carbon matrix and corresponding elemental analysis depicted high N content of *ca.* 5.3 wt %, which was also confirmed by the CHN elemental analysis. From the CHN elemental analysis, the contents of C, H, and N were found to be 87.76, 0.13, and 4.97 wt %, respectively. The high-resolution TEM (HRTEM) analysis of Ru-PAL-800 (Figure 2a) shows a nanoporous structure (<1

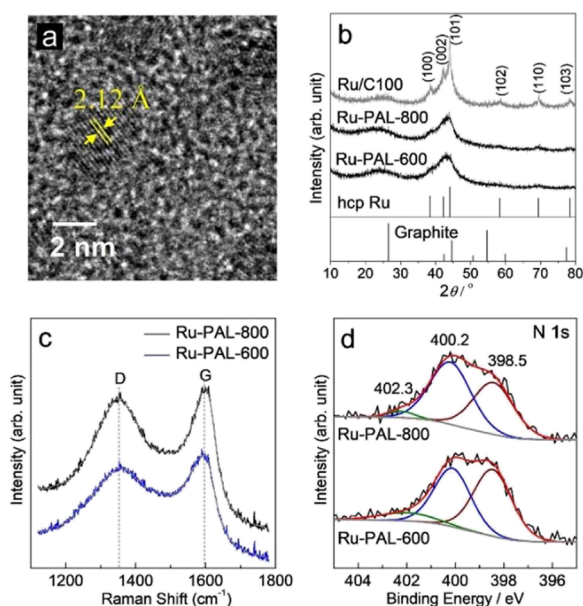
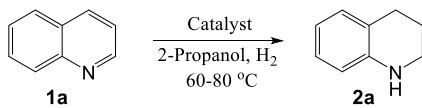


Figure 2. (a) HRTEM image of Ru-PAL-800. (b) XRD patterns of Ru-PAL-*x* and Ru/C100. JCPDF card numbers are (hcp Ru) 00-006-0663 and (graphite) 00-023-0064. (c) Raman spectra of Ru-PAL-*x*. (d) XPS spectra recorded on N 1s region for Ru-PAL-*x*. Ru-PAL-*x* ($R_{\text{PAL/Ru}} = 12$) samples are prepared at pH 1.

nm micropores) of N-carbon hybrid incorporating the Ru NPs. The N_2 sorption analysis of Ru-PAL-800 (Figure S4) also depicted characteristic type-I isotherms of microporous solids,^{50,55} giving noticeably high BET surface area up to 652 $\text{m}^2 \text{g}^{-1}$ (Tables S1 and S2). In Figure 2a, the lattice spacing in the flat Ru patches was found to be 2.12 Å, which is close to that ($d_{002} = 2.142 \text{ \AA}$) of the hexagonal-close-packed (hcp) (002) plane of Ru.^{10,56} This was also supported by the powder X-ray diffraction (XRD) patterns of Ru-PAL-*x* (Figure 2b), displaying broad diffraction peaks corresponding to hcp Ru

particles, which remained stable in the support with the increase of the pretreatment temperature from 600 to 800 °C. The Raman spectra suggested the formation of graphitic carbon in Ru-PAL-*x* (Figure 2c), in which the G band ($\sim 1590 \text{ cm}^{-1}$) appeared for the in-plane vibration of sp^2 carbon atoms, while the D band ($\sim 1350 \text{ cm}^{-1}$) is a defect-induced Raman feature describing the nonperfect crystalline structure.^{25,44} The broad and strong D band indicates amorphization of the graphitic network due to the defect that arises from high N content, which is also in agreement with the weak XRD peak at $\sim 26.0^\circ$ for poor graphitic stacking. The nature of N-doping in Ru-PAL-*x* was examined by the XPS spectra in the N 1s region (Figure 2d). The deconvoluted XPS spectra can be assigned to three different types of nitrogen, namely, pyridinic N (398.5 eV), pyrrolic N (400.2 eV), and NO_x species (402.3 eV).^{25,51} A high content of pyridinic N and pyrrolic N (43.0 vs 42.2% at 600 °C and 39.8 vs 54.9% at 800 °C) was found, which is effective for inducing large defects in the graphitic network due to the terminal N-atoms.⁴³ The lone pair electrons of pyridinic N and pyrrolic N can serve as strong metal binding sites,^{57,58} which could be attributable for stabilizing the highly dispersed small Ru NPs. The growth of Ru clusters was perhaps mostly confined around the N-sites of the Ru/PAL composite (Figure 1A) during pyrolysis, which effectively produces ultra-small NPs. In a contrast, the control sample Ru/C100 (without any N-functionalities) shows deposition of relatively larger Ru NPs on carbon with a mean Ru particle size of *ca.* 3.0 nm (Figure S5), which was also indicated from the XRD pattern (Figure 2b).

Catalytic Hydrogenation of Quinoline as a Model N-Heteroarene. The conversion of quinoline (1a) to 1,2,3,4-tetrahydroquinoline (2a) was selected as a model reaction to investigate the hydrogenation of N-heteroarenes over Ru-PAL-*x* catalysts. The hydrogenation of 1a to 2a often produces the benzene ring hydrogenation product 5,6,7,8-tetrahydroquinoline (3a) and the complete hydrogenation product decahydroquinoline (4a) over most of the heterogeneous Ru catalysts (Table S3). Initial hydrogenation reaction in 2-propanol under 1 MPa of H_2 at 80 °C showed Ru-PAL-800 as the most active catalyst among the Ru-PAL-*x* pretreated at 600–900 °C (Table 1, entry 1–4), which provided a quantitative 2a yield (99%; TOF: 54 h^{-1}) in 8 h. With the increase of H_2 pressure, the formation rate of 2a increased rapidly (Figure 3a), giving 93% yield (TOF: 158 h^{-1}) of 2a in only 2 h under 3 MPa H_2 at 80 °C, without any significant decrease of its high selectivity. The Ru-PAL-800 is also effective under milder reaction condition, affording selective 2a formation with a yield (in 8 h) of 78% (TOF: 43 h^{-1}) and 62% (TOF: 34 h^{-1}) at 60 °C under 1 and 0.5 MPa of H_2 , respectively (Table 1, entry 5–6; Figure S6). Next, in the presence of Ru-PAL-800, the influence of the solvent was investigated (Table S4). An excellent yield of 2a (94–98%) with high selectivity (98–99%) in 8 h catalysis was also achieved by using ethanol, methanol, and toluene, whereas in 1,4-dioxane, THF and CH_3CN , moderate catalytic activity (59–74% yield and 83–91% selectivity of 2a) was observed. Negligible conversion of 1a was observed over Ru-PAL-800 in 2-propanol for the reaction under 2 MPa of Ar instead of H_2 , which excludes transfer hydrogenation with the alcohol solvent (Table S4, entry 8). Interestingly, without any solvent, 2a is obtained in excellent yield (96%) and selectivity (98%) in 6 h with a TOF of 167 h^{-1} (Table 1, entry 7), which is twice faster in rate than that over an efficient catalyst of Ru/

Table 1. Catalytic Performance for Hydrogenation of 1a over Various Ru Catalysts^a


entry	catalyst ^b	T (°C)	2a yield ^c (%)	2a sel (%)	TOF ^d (h ⁻¹)
1	Ru-PAL-600	80	56	97	27
2	Ru-PAL-700	80	73	96	33
3	Ru-PAL-800	80	99	99	54 ^h
4	Ru-PAL-900	80	86	91	42
5	Ru-PAL-800	60	78	98	43 ^h
6 ^e	Ru-PAL-800	60	62	99	34 ^h
7 ^f	Ru-PAL-800	80	96	98	167
8	Ru/C-com	80	47	73	43 ^h
9	Ru/C100	80	36	68	38 ^h
10 ^g	Ru-HCP	80	29	74	39
11	Ru/SiO ₂	80	34	52	20
12	Ru/TiO ₂	80	23	60	12
13	Ru/Nb ₂ O ₅	80	12	71	14
14	Ru/CeO ₂	80	28	59	
15	Ru/Al ₂ O ₃	80	21	74	24

^aReaction conditions: catalyst (Ru: ~5 wt %) 5 mg, 0.5 mmol **1a**, 2 mL of 2-propanol, 1.0 MPa H₂, 60–80 °C, 8 h. ^bRu-PAL-*x* (*x*: pretreatment temperature in °C). ^cDetermined by GC using chlorobenzene as an internal standard. ^dTOF was calculated from the dispersion of surface Ru atoms determined by CO chemisorption. ^eReaction was performed under 0.5 MPa H₂. ^fWithout solvent reaction conditions: catalyst (Ru: ~5 wt %) 16 mg, 5 mmol **1a**, 1.0 MPa H₂, 80 °C, 6 h. ^gReaction was performed with 0.25 mg of catalyst (pristine Ru) to balance Ru amount. ^hTOF was calculated from 2a yield at 1 h.

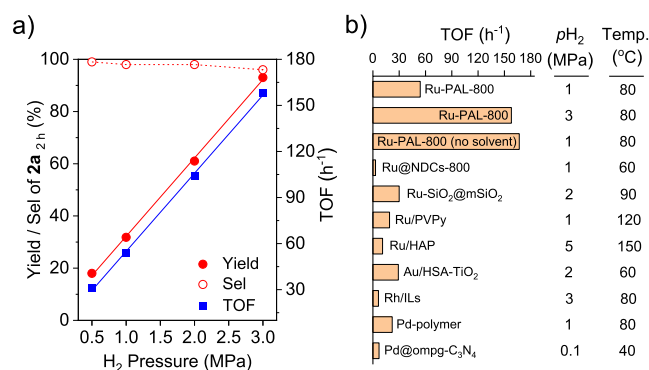


Figure 3. (a) Effect of H₂ pressure on the conversion of **1a** to **2a** over Ru-PAL-800. Reaction conditions: catalyst (5 mg), **1a** (0.5 mmol), 2-propanol (2 mL), 0.5–3.0 MPa H₂, 80 °C, 2 h. (b) Comparison of TOF for conversion of **1a** to **2a** over Ru-PAL-800 with reported noble metal catalysts. Details of different noble metal catalysts and reaction conditions are provided in Table S5.

HT-C12A7 (98% **2a** yield in 12 h) under the same catalysis condition (Table S5, entry 4).³³

The catalytic performances for hydrogenation of **1a** over Ru-PAL-800 were compared with different Ru catalysts, namely, Ru NPs on a carbon support (commercial Ru/C-com and Ru/C100), pristine hcp Ru NPs (Ru-HCP), and different supported Ru catalysts (Ru/support; support = SiO₂, TiO₂, Nb₂O₅, CeO₂ and Al₂O₃), with the yield of **2a** did not even reach 50% (selectivity below 75%) at 8 h (Table 1, entry 8–15) with significant formation of **3a** (selectivity, 5–11%) and

4a (selectivity, 18–42%) (Table S3, entry 8–15). Figure 4a shows the time course of the reaction over different Ru

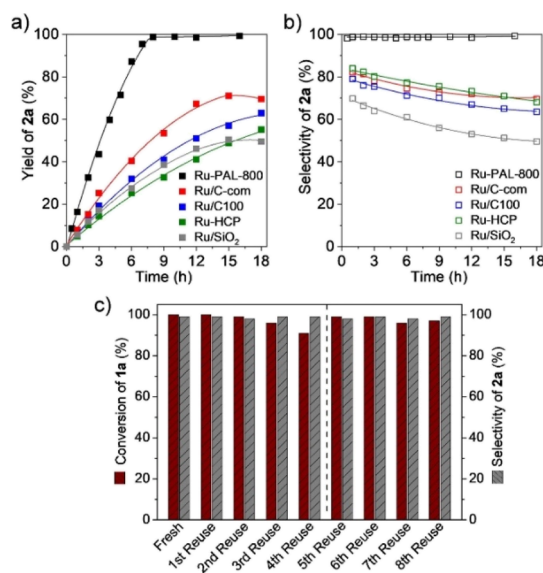


Figure 4. (a) Product yield/time and (b) selectivity/time profiles of hydrogenation of **1a** to **2a** over different Ru catalysts. (c) Reuse experiment of Ru-PAL-800 for hydrogenation of **1a** to **2a** after 8 h catalysis. After 4th reuse, catalysts were recovered from two different reused batches and 5 mg of sample was used for 5th reuse. Reaction conditions: catalyst (5 mg, Ru: ~5 wt %; for Ru-HCP 0.25 mg), **1a** (0.5 mmol), 2-propanol (2 mL), and H₂ (1 MPa), 80 °C.

catalysts. Formation of **2a** over Ru-PAL-800 was completed quantitatively at approximately 8 h with no detection of **3a** and **4a**. Selectivity of **2a** was not decreased even after 16 h of catalysis (Figure 4b). In a sharp contrast, **2a** was formed with approximately 2–4 times lower rate over other tested catalysts (Ru/C-com, Ru/C100, Ru-HCP, and Ru/SiO₂), which took over 15 h for the complete conversion of **1a** (Figure S7) with a **2a** yield of 50–70% at 18 h. Moreover, the selectivity of **2a** decreases with time due to concurrent benzene ring hydrogenation. Ru-PAL-800 exhibited markedly higher catalytic activity within the shorter reaction time and/or under much milder reaction conditions (even with lower metal/**1a** ratio used for the reaction) than other efficient noble metal catalysts reported to date for hydrogenation of **1a** to produce **2a** (Table S5),^{26,27,32,33,36,51} except for few catalysts based on highly expensive Pd^{23,25} (5–9 times higher metal/**1a** ratio than Ru-PAL-800 was used; Table S5, entry 16 and 18). To the best of our knowledge, Ru-PAL-800 exhibited 5–24-fold higher TOF up to ca. 167 h⁻¹, among the reported efficient metal catalysts for hydrogenation of **1a** to **2a** (Figure 3b; see Table S5 for detail comparison).

Reuse experiments were conducted to determine the durability of Ru-PAL-800 catalyst (Figure 4C). Both catalytic activity and chemoselectivity became markedly well retained even after eight reuses. High reusability of Ru-PAL-800 catalyst was also confirmed in an incomplete conversion condition of 2 h catalysis (Figure S8). No noticeable change in the structure of the reused catalyst was observed as depicted by the XRD and XPS analysis (Figure S9). The XPS spectra in the N 1s region (Figure S9c) revealed that there is no substantial change in the nature of N-species on the surface of the reused catalyst, which implies that **1a** or **2a** were not adsorbed on the catalyst

surface. Elemental analysis also depicted that there is no significant difference in N content in the fresh and eighth reused catalysts (4.97 and 4.81 wt %, respectively). These results indicate the high resistance of Ru-sites of Ru-PAL-800 from poisoning by the N atom of **1a** or **2a** through strong coordination (*vide infra*).^{29,34} In a sharp contrast, **2a** yield was decreased drastically by 38 and 33% even after the second reuse of Ru/C-com and Ru/C100 catalysts, respectively (Figure S10).

Electronic Properties of Ru for High-Performance Catalysis. The efficient catalytic performance of Ru-PAL-800 cannot be merely attributed to the morphology (sub-nanometer Ru particles and high surface area) because Ru/C-Com is catalytically much inferior to Ru-PAL-800 even with higher surface area (Table S2). Recently, it has been revealed that the electronic properties of Ru in both pristine and metal-oxide supported catalysts greatly influence the reaction rate and/or selectivity for reductive amination^{3,7} and ammonia synthesis.^{4,38} To recognize the electronic properties of the present Ru-based system and its effect in catalytic hydrogenation, the electronic state of Ru NPs in Ru-PAL-800, Ru/C100, and Ru-HCP was investigated by diffuse reflectance infrared Fourier transform (DRIFT) spectroscopy using CO as a probe molecule (Figure 5). The bands were assigned to the

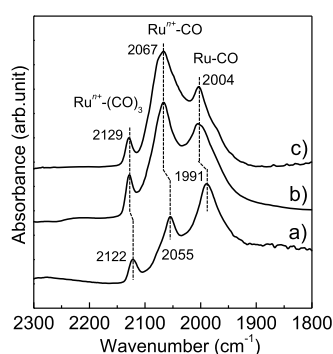


Figure 5. Difference DRIFT spectra for adsorption of CO onto (a) Ru-PAL-800, (b) Ru/C100, and (c) Ru-HCP samples at 103 K.

C–O stretching vibration of linearly adsorbed CO on Ru⁰ [Ru⁰–CO; 1991–2004 cm^{−1}], linearly adsorbed CO on partially oxidized Ru [Ruⁿ⁺–CO; 2055–2067 cm^{−1}], and tricarbonyl species on partially oxidized Ru [Ruⁿ⁺–(CO)₃; 2022–2029 cm^{−1}].^{59,60} The bands (1991, 2055, and 2122 cm^{−1}) observed for Ru-PAL-800 were red-shifted than those (2004, 2067, and 2129 cm^{−1}) for Ru/C100 and Ru-HCP, which indicate an increase of electron density of Ru in Ru-PAL-800, due to electron donation from the filled π -orbital of N-atoms of the N-carbon support to the empty d-orbital of Ru,⁴² thereby weakening the C≡O bond by back-donation of electrons from Ru to the 2 π^* antibonding orbitals of CO. Absence of any electronic interaction between Ru and carbon support of Ru/C100 was confirmed by its bands at an identical position of pristine Ru-HCP. Moreover, a larger fraction of metallic Ru was present in Ru-PAL-800 compared to Ru/C100 and Ru-HCP as indicated from the higher intensity of Ru⁰–CO band than Ruⁿ⁺–CO and Ruⁿ⁺–(CO)₃ for Ru-PAL-800, which is also in agreement with the XPS results. A Ru-PAL-800 (prepared at pH 9) catalyst also shows red-shift of the bands due to strong electron-donating ability but with much lower intensity of Ru⁰–CO relative to Ruⁿ⁺–CO and Ruⁿ⁺–(CO)₃

signals (Figure S11) due to partly reduced metal surface (also confirmed by XPS), providing selective formation of **2a** but with \sim 4-fold lower reaction rate (Table S3, entry 7). Hence, the electron-rich metallic Ru is considered to play an important role as active sites, which promoted the highly efficient and selective hydrogenation of **1a** by strong electron-donating power. The strong electronic interaction of pyridinic N and pyrrolic N with very small-sized Ru NPs is attributable for efficient charge transfer from the N-carbon support, resulting in the strong electron donating power of the Ru sites.

Computational Studies for the Atomistic Insight of High-Performance Catalysis. We have performed the first-principles-based calculations under the framework of density functional theory (DFT) to explore the atomistic insight of the present catalytic system. As a first step, we have modelled a flat-shaped hcp Ru(002) nanocluster supported on top of the N-carbon frame (Figure S12). The structure was fully relaxed and following this on analyzing the Hirshfeld charge density, we have found that N-atoms of the support were bound strongly with the Ru atoms through electron donation, thereby increasing the negative charge density of the Ru(002) surface. This observation is in good agreement with our DRIFT spectroscopic results.

Next, we have estimated the adsorption energies (E_{ad}) of the quinoline (**1a**) molecule on top of a neutral Ru(002) nanocluster and compared the same with a negatively charged Ru ^{δ^-} (002) nanocluster. Note that the latter is our representative model system of the Ru nanocluster on the N-carbon system. The different adsorbed configurations of **1a** molecule on Ru(002) and Ru ^{δ^-} (002) surfaces are shown in Figure 6.⁶¹ The most stable configuration for **1a** entails both

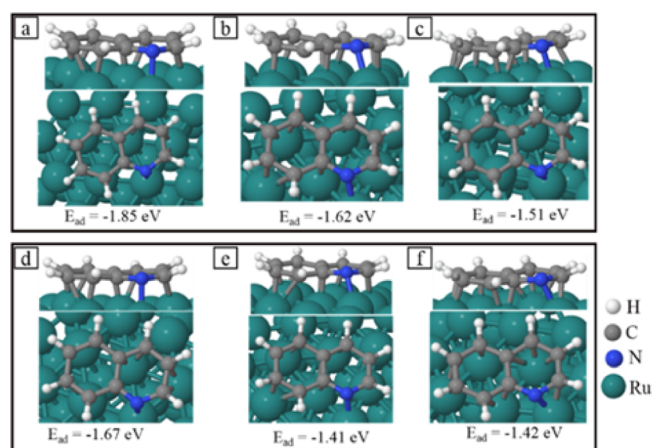


Figure 6. Side and top view of DFT-optimized adsorption configurations of **1a** on neutral Ru(002) nanocluster (a,b,c) and negatively charged Ru ^{δ^-} (002) nanocluster (d,e,f). The adsorption energy (E_{ad}) of **1a** is shown with respective configuration.

rings lying flat on the surface and N-atom centered on Ru atom. **1a** adsorbs on the Ru(002) surface with an overall higher E_{ad} of -1.51 to -1.85 eV (Figure 6a–c) (depending on the site of the nanocluster). The E_{ad} for Ru ^{δ^-} (002) surface is -1.41 to -1.67 eV (Figure 6d,e) for all possible configurations. This reduction in E_{ad} reveals the weak interaction of the N-heterocyclic ring of **1a** with the Ru ^{δ^-} (002) surface, which prevents the poisoning of the catalyst^{29,34} as evidenced from the excellent recyclability of the Ru-PAL-800.

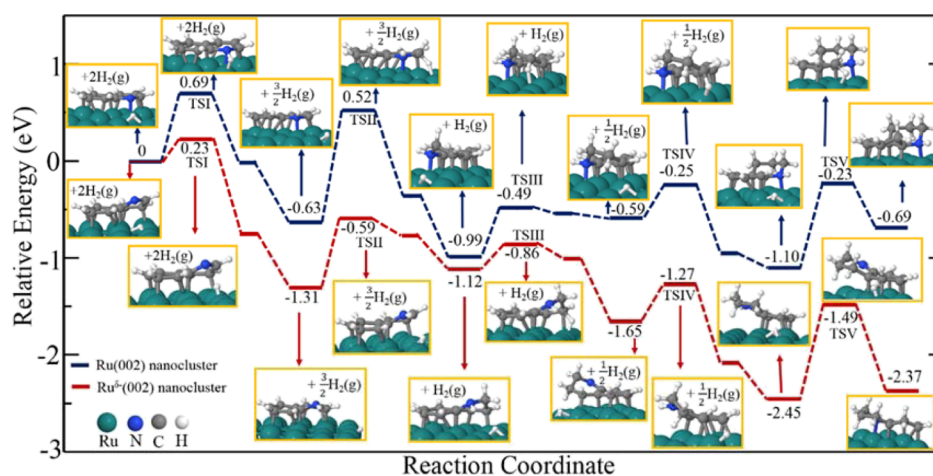


Figure 7. Computational studies for the reaction profile for the conversion of quinoline (**1a**) to 1,2,3,4-tetrahydroquinoline (**2a**). The side view of initial state (IS), transition state (TS), and final state (FS) structures of all the elementary steps on neutral Ru(002) and negatively charged Ru $\delta^-(002)$ nanocluster are shown.

To ensure the reason for efficient catalysis, the energy barriers of elementary steps of **1a** hydrogenation over Ru(002) and Ru $\delta^-(002)$ surfaces were calculated, and the corresponding reaction paths were obtained (Figure 7). All the free energies were set from a reference of **1a** with one adsorbed H-atom on Ru and two H₂ molecules in the gaseous phase. It is important to note that on top of the Ru cluster, the H₂ molecule gets dissociated into atomic H, which further takes part in the hydrogenation steps (Figure S13).⁶² The activation barrier (E_a ; Table 2) reacting on the first H-atom to the N-

Table 2. Energy Barriers (E_a) of the Elementary Steps for Hydrogenation of **1a** on Neutral Ru(002) and Negatively Charged Ru $\delta^-(002)$ Nanocluster

hydrogenation steps ^a	energy barrier height (eV)	
	Ru(002)	Ru $\delta^-(002)$
1st	0.69	0.23
2nd	1.15	0.72
3rd	0.50	0.26
4th	0.38	0.34
benzene ring hydrogenation	0.87	0.96

^aHydrogenation steps for N-heterocyclic ring of **1a**.

atom of the heterocyclic ring (step I) on the Ru surface is smaller on Ru $\delta^-(002)$ (~0.23 eV) than that on Ru(002) (~0.69 eV). This clearly indicates the facile reduction of the N-atom with more localized negative charge density. Also, the next consecutive step (II) of hydrogenation proceeds easily on Ru $\delta^-(002)$ (having $E_a \sim 0.72$ eV; Table 2), due to the weak interaction of the adjacent C-atom of the N-heterocyclic ring with the Ru surface. Owing to these hydrogenation steps, the N-heterocyclic ring was observed to get tilted (some part is displaced upward) from the surface in such a way that the interaction with the Ru surface becomes weaker than before. We find this to be more significant on Ru $\delta^-(002)$ nanocluster than on the neutral counterpart. Since on the Ru $\delta^-(002)$ surface, some part of the N-heterocyclic gets more tilted, the C-atom's interaction gets reduced with the Ru atoms, which results in favorable hydrogenation. Moreover, the adjacent H-atom (dissociative adsorbed H-atom) could move easily on the Ru surface to reach the C-atom of the N-heterocyclic ring

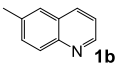
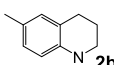
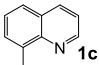
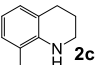
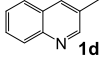
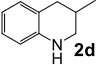
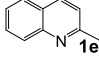
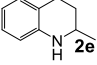
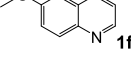
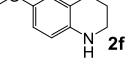
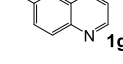
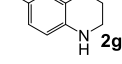
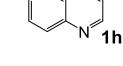
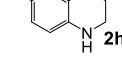
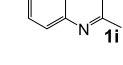
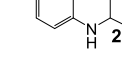
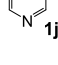
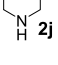
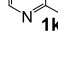
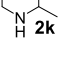
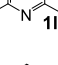
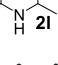
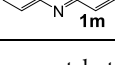
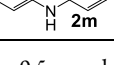
(Figure S14 and Note S5). This helps in turn to have lesser activation barrier E_a for the next two steps (III and IV) of the hydrogenation on the Ru $\delta^-(002)$ surface (Table 2). However, note that the activation barrier for the hydrogenation of step (V) of the benzene ring was observed to be higher on the Ru $\delta^-(002)$ surface (Table 2) than on the neutral one. This infers that there is a preferential selective hydrogenation of the N-heterocyclic ring of **1a** on the Ru $\delta^-(002)$ surface. The lower E_a for hydrogenation of the N-heterocyclic ring is ascribed to its weak interaction with the electron-rich Ru surface, which results in the high performance of the present catalytic system.

Scope of Selective Hydrogenation of Various N-Heteroarenes. Several quinoline derivatives with reduction sensitive functional groups, such as alkyl substituents, alkoxy, and halogens were successfully tolerated over Ru-PAL-800 (Table 3, entries 1–8), which is readily converted to corresponding 1,2,3,4-tetrahydroquinolines in high yields and selectivity, irrespective of the electronic effects from the functional groups. Noticeably, the quinolines bearing chlorine and fluorine atoms are smoothly hydrogenated without the formation of any dehalogenation products (Table 3, entries 6–8).^{27,28} The present catalytic system is also effective for hydrogenation of pyridines to the corresponding piperidines, which are important structural motif in many chemical products and synthetic drugs.^{15,16} Although, hydrogenation of the less active pyridines often required harsh reaction conditions (high temperature and/or high H₂ pressure),^{15,26} Ru-PAL-800 efficiently produced several piperidines (Table 3, entries 9–11) under mild conditions. Other, N-heteroarene such as acridine (Table 3, entries 12) was also hydrogenated selectively. In a contrast, a Ru catalyst supported on carbon (Ru/C100) provided 2.4–4.1 times lower yields of hydrogenated products of different N-heteroarenes with very low selectivity when compared with the Ru-PAL-800 (Table 3).

CONCLUSIONS

In summary, we have developed a high-performance catalytic hydrogenation system based on a novel Ru nanocomposite, comprising electron-rich small Ru NPs immobilized on a high-surface-area N-carbon. A practical and scalable synthesis strategy was demonstrated by using an easily designed self-assembly of RuCl₃ and a N-functional structure-directing

Table 3. Comparison of Hydrogenation of Various N-Heteroarenes Over the Ru-PAL-800 and Ru/C100 Catalysts^a

Entry	Substrate	Time (h)	Product	Yield ^b (Sel) (%)		R _{Ru-PAL-800} ^c
				Ru-PAL-800	Ru/C100	
1		10		95 (96)	29 (58)	3.3
2		10		97 (98)	33 (61)	2.9
3		8		93 (94)	24 (53)	3.9
4		8		96 (96)	27 (52)	3.6
5		10		91 (93)	22 (45)	4.1
6		8		93 (94)	31 (51)	3.0
7		8		95 (95)	33 (56)	2.9
8		8		89 (91)	26 (43)	3.4
9		12		99 (99)	41 (96)	2.4
10		12		95 (99)	35 (97)	2.7
11		12		96 (99)	33 (96)	2.9
12		8		98 (99)	28 (47)	3.5

^aReaction conditions: catalyst (Ru: ~5 wt %) 5 mg, 0.5 mmol substrate, 2 mL of 2-propanol, 1.0 MPa H₂, 80 °C. ^bGC yield. ^cR_{Ru-PAL-800} defined the ratio of product yields for Ru-PAL-800 and Ru/C100.

ligand PAL, *via* pyrolysis/pretreatment. The strong electron donating power of Ru sites is ascribed to the efficient electronic interaction of small-sized Ru NPs with the abundant pyridinic N and pyrrolic N present in N-carbon support. The synergistically controlled NP morphology, surface area, and electronic properties of the present catalyst provided outstanding catalytic performance under mild conditions for chemoselective hydrogenation of several N-heteroarenes. The catalyst exhibits excellent durability from poisoning by N atom of heterocycles during prolonged recycling, which is due to the weak adsorption energies at the electron-rich Ru surface as evident from DFT calculations. DFT calculations further reveal that the low activation barriers for hydrogenation steps of the N-heterocyclic ring of quinoline was the origin of high catalytic performance. The present material is expected to be widely applicable for several indispensable catalytic hydrogenation

reactions as well as promising for different catalysis technologies including electrocatalysis, where electronic properties of metal-centers have strong influence on the catalytic performance.

■ ASSOCIATED CONTENT

SI Supporting Information

The Supporting Information is available free of charge at <https://pubs.acs.org/doi/10.1021/acsami.0c15407>.

Experimental detail, five tables, surface area and catalytic property optimization data, XPS spectra, XRD patterns, N₂ sorption isotherm, STEM image, time-course of hydrogenation, different catalysts reusability data, DRIFT spectra, DFT optimized configurations, and characterization of obtained compounds (PDF)

AUTHOR INFORMATION

Corresponding Authors

Debraj Chandra – World Research Hub Initiative (WRHI), Institute of Innovative Research, Tokyo Institute of Technology, Yokohama 226-8503, Japan; orcid.org/0000-0002-5408-5092; Email: chandra.d.aa@m.titech.ac.jp

Saswata Bhattacharya – Department of Physics, Indian Institute of Technology Delhi, New Delhi 110016, India; orcid.org/0000-0002-4145-4899; Email: saswata@physics.iitd.ac.in

Michikazu Hara – Laboratory for Materials and Structures, Institute of Innovative Research, Tokyo Institute of Technology, Yokohama 226-8503, Japan; Advanced Low Carbon Technology Research and Development Program (ALCA), Japan Science and Technology Agency (JST), Kawaguchi, Saitama 332-0012, Japan; orcid.org/0000-0003-3450-5704; Email: mhara@msl.titech.ac.jp

Authors

Shikha Saini – Department of Physics, Indian Institute of Technology Delhi, New Delhi 110016, India

Asim Bhaumik – School of Materials Sciences, Indian Association for the Cultivation of Science, Kolkata 700 032, India

Keigo Kamata – Laboratory for Materials and Structures, Institute of Innovative Research, Tokyo Institute of Technology, Yokohama 226-8503, Japan; orcid.org/0000-0002-0624-8483

Complete contact information is available at: <https://pubs.acs.org/10.1021/acsami.0c15407>

Author Contributions

D.C. and M.H. designed the research. D.C. performed the synthesis, structural characterizations, and catalytic tests. S.S. and S.B. performed the computational studies. A.B. and K.K. contributed to the discussion and analysis of the results. The manuscript was constructed by D.C. Computational part was written by S.B. All authors discussed the results and commented on the manuscript.

Notes

The authors declare no competing financial interest.

ACKNOWLEDGMENTS

This work was supported by a fund from the Grants-in-Aid for Japan Society for the Promotion of Science (JSPS) Fellows and for Scientific Research from the Ministry of Education, Culture, Science, Sports, and Technology (MEXT) of Japan (18H05251). S.S. acknowledges CSIR, India, for the senior research fellowship [grant no. 09/086(1231)2015-EMR-I]. S.B. acknowledges the core research grant from SERB research grant, DST, India (grant no. CRG/2019/000647). S.B. and S.S. acknowledge the High Performance Computing (HPC) facility at IIT Delhi for computational resources.

REFERENCES

(1) Munnik, P.; de Jongh, P. E.; de Jong, K. P. Recent Developments in the Synthesis of Supported Catalysts. *Chem. Rev.* **2015**, *115*, 6687–6718.

(2) He, L.; Weniger, F.; Neumann, H.; Beller, M. Synthesis, Characterization, and Application of Metal Nanoparticles Supported on Nitrogen-Doped Carbon: Catalysis beyond Electrochemistry. *Angew. Chem., Int. Ed.* **2016**, *55*, 12582–12594.

(3) Chandra, D.; Inoue, Y.; Sasase, M.; Kitano, M.; Bhaumik, A.; Kamata, K.; Hosono, H.; Hara, M. A High Performance Catalyst of Shape-Specific Ruthenium Nanoparticles for Production of Primary Amines by Reductive Amination of Carbonyl Compounds. *Chem. Sci.* **2018**, *9*, 5949–5956.

(4) Kitano, M.; Inoue, Y.; Yamazaki, Y.; Hayashi, F.; Kanbara, S.; Matsuishi, S.; Yokoyama, T.; Kim, S.-W.; Hara, M.; Hosono, H. Ammonia Synthesis using a Stable Electride as an Electron Donor and Reversible Hydrogen Store. *Nat. Chem.* **2012**, *4*, 934–940.

(5) Vajda, S.; Pellin, M. J.; Greeley, J. P.; Marshall, C. L.; Curtiss, L. A.; Ballentine, G. A.; Elam, J. W.; Catillon-Mucherie, S.; Redfern, P. C.; Mehmood, F.; Zapol, P. Subnanometre Platinum Clusters as Highly Active and Selective Catalysts for the Oxidative Dehydrogenation of Propane. *Nat. Mater.* **2009**, *8*, 213–216.

(6) Chen, L.-W.; Tong, L.; Nan, H.; Chu, S.-Q.; Liang, H.-W. Sub-2 nm Ir Nanoclusters Immobilized on Mesoporous Nitrogen-Doped Carbons as Efficient Catalysts for Selective Hydrogenation. *ACS Appl. Nano Mater.* **2019**, *2*, 6546–6553.

(7) Komanoya, T.; Kinemura, T.; Kita, Y.; Kamata, K.; Hara, M. Electronic Effect of Ruthenium Nanoparticles on Efficient Reductive Amination of Carbonyl Compounds. *J. Am. Chem. Soc.* **2017**, *139*, 11493–11499.

(8) Claus, P.; Brückner, A.; Mohr, C.; Hofmeister, H. Supported Gold Nanoparticles from Quantum Dot to Mesoscopic Size Scale: Effect of Electronic and Structural Properties on Catalytic Hydrogenation of Conjugated Functional Groups. *J. Am. Chem. Soc.* **2000**, *122*, 11430–11439.

(9) Karim, A. M.; Prasad, V.; Mpourmpakis, G.; Lonergan, W. W.; Frenkel, A. I.; Chen, J. G.; Vlachos, D. G. Correlating Particle Size and Shape of Supported Ru/ γ -Al₂O₃ Catalysts with NH₃ Decomposition Activity. *J. Am. Chem. Soc.* **2009**, *131*, 12230–12239.

(10) Yin, A.-X.; Liu, W.-C.; Ke, J.; Zhu, W.; Gu, J.; Zhang, Y.-W.; Yan, C.-H. Ru Nanocrystals with Shape-Dependent Surface-Enhanced Raman Spectra and Catalytic Properties: Controlled Synthesis and DFT Calculations. *J. Am. Chem. Soc.* **2012**, *134*, 20479–20489.

(11) Campbell, C. T. Electronic Perturbations. *Nat. Chem.* **2012**, *4*, 597–598.

(12) Newton, M. A.; Belver-Coldeira, C.; Martínez-Arias, A.; Fernández-García, M. Dynamic in situ Observation of Rapid Size and Shape Change of Supported Pd Nanoparticles During CO/NO Cycling. *Nat. Mater.* **2007**, *6*, 528–532.

(13) Wang, D.-S.; Chen, Q.-A.; Lu, S.-M.; Zhou, Y.-G. Asymmetric Hydrogenation of Heteroarenes and Arenes. *Chem. Rev.* **2012**, *112*, 2557–2590.

(14) Wiesenfeldt, M. P.; Nairoukh, Z.; Dalton, T.; Glorius, F. Selective Arene Hydrogenation for Direct Access to Saturated Carbo- and Heterocycles. *Angew. Chem., Int. Ed.* **2019**, *58*, 10460–10476.

(15) Chen, F.; Li, W.; Sahoo, B.; Kreyenschulte, C.; Agostini, G.; Lund, H.; Junge, K.; Beller, M. Hydrogenation of Pyridines Using a Nitrogen-Modified Titania-Supported Cobalt Catalyst. *Angew. Chem., Int. Ed.* **2018**, *57*, 14488–14492.

(16) Hegedűs, L.; Háda, V.; Tungler, A.; Máthé, T.; Szepeszy, L. Diastereoselective Heterogeneous Catalytic Hydrogenation of N-Heterocycles. Part I. Hydrogenation of Pyridines. *Appl. Catal., A* **2000**, *201*, 107–114.

(17) He, Y.-M.; Song, F.-T.; Fan, Q.-H. Advances in Transition Metal-Catalyzed Asymmetric Hydrogenation of Heteroaromatic Compounds. In *Stereoselective Formation of Amines*; Li, W., Zhang, X., Eds.; Topics in Current Chemistry, 2014; Vol. 343; pp 145–190.

(18) Duan, Y.-N.; Du, X.; Cui, Z.; Zeng, Y.; Liu, Y.; Yang, T.; Wen, J.; Zhang, X. Homogeneous Hydrogenation with a Cobalt/Tetraphosphine Catalyst: A Superior Hydride Donor for Polar Double Bonds and N-Heteroarenes. *J. Am. Chem. Soc.* **2019**, *141*, 20424–20433.

(19) Sridharan, V.; Suryavanshi, P. A.; Menéndez, J. C. Advances in the Chemistry of Tetrahydroquinolines. *Chem. Rev.* **2011**, *111*, 7157–7259.

(20) Wu, C.; Liao, J.; Ge, S. Cobalt-Catalyzed Enantioselective Hydroboration/Cyclization of 1,7-Enynes: Asymmetric Synthesis of

Chiral Quinolinones Containing Quaternary Stereogenic Centers. *Angew. Chem., Int. Ed.* **2019**, *58*, 8882–8886.

(21) Sahoo, B.; Kreyenschulte, C.; Agostini, G.; Lund, H.; Bachmann, S.; Scalone, M.; Junge, K.; Beller, M. A Robust Iron Catalyst for the Selective Hydrogenation of Substituted (Iso)-Quinolinones. *Chem. Sci.* **2018**, *9*, 8134–8141.

(22) Zhang, S.; Xia, Z.; Ni, T.; Zhang, Z.; Ma, Y.; Qu, Y. Strong Electronic Metal-Support Interaction of Pt/CeO₂ Enables Efficient and Selective Hydrogenation of Quinolines at Room Temperature. *J. Catal.* **2018**, *359*, 101–111.

(23) Gong, Y.; Zhang, P.; Xu, X.; Li, Y.; Li, H.; Wang, Y. A Novel Catalyst Pd@ompg-C₃N₄ for Highly Chemoselective Hydrogenation of Quinoline Under Mild Conditions. *J. Catal.* **2013**, *297*, 272–280.

(24) Zhang, Y.; Zhu, J.; Xia, Y.-T.; Sun, X.-T.; Wu, L. Efficient Hydrogenation of Nitrogen Heterocycles Catalyzed by Carbon-Metal Covalent Bonds-Stabilized Palladium Nanoparticles: Synergistic Effects of Particle Size and Water. *Adv. Synth. Catal.* **2016**, *358*, 3039–3045.

(25) Hu, X.; Chen, Y.; Huang, B.; Liu, Y.; Huang, H.; Xie, Z. Pd-Supported N/S-Codoped Graphene-Like Carbons Boost Quinoline Hydrogenation Activity. *ACS Sustainable Chem. Eng.* **2019**, *7*, 11369–11376.

(26) Karakulina, A.; Gopakumar, A.; Akçok, İ.; Roulier, B. L.; LaGrange, T.; Katsyuba, S. A.; Das, S.; Dyson, P. J. A Rhodium Nanoparticle–Lewis Acidic Ionic Liquid Catalyst for the Chemoselective Reduction of Heteroarenes. *Angew. Chem., Int. Ed.* **2016**, *55*, 292–296.

(27) Ren, D.; He, L.; Yu, L.; Ding, R.-S.; Liu, Y.-M.; Cao, Y.; He, H.-Y.; Fan, K.-N. An Unusual Chemoselective Hydrogenation of Quinoline Compounds Using Supported Gold Catalysts. *J. Am. Chem. Soc.* **2012**, *134*, 17592–17598.

(28) Zhang, S.; Xia, Z.; Ni, T.; Zhang, H.; Wu, C.; Qu, Y. Tuning Chemical Compositions of Bimetallic AuPd Catalysts for Selective Catalytic Hydrogenation of Halogenated Quinolines. *J. Mater. Chem. A* **2017**, *5*, 3260–3266.

(29) Zhu, D.; Jiang, H.; Zhang, L.; Zheng, X.; Fu, H.; Yuan, M.; Chen, H.; Li, R. Aqueous Phase Hydrogenation of Quinoline to Decahydroquinoline Catalyzed by Ruthenium Nanoparticles Supported on Glucose-Derived Carbon Spheres. *ChemCatChem* **2014**, *6*, 2954–2960.

(30) Konnerth, H.; Precht, M. H. G. Selective Hydrogenation of N-Heterocyclic Compounds Using Ru Nanocatalysts in Ionic Liquids. *Green Chem.* **2017**, *19*, 2762–2767.

(31) Fang, M.; Sánchez-Delgado, R. A. Ruthenium Nanoparticles Supported on Magnesium Oxide: A Versatile and Recyclable Dual-Site Catalyst for Hydrogenation of Mono- and Poly-Cyclic Arenes, N-Heteroarenes, and S-Heteroarenes. *J. Catal.* **2014**, *311*, 357–368.

(32) Wang, X.; Chen, W.; Zhang, L.; Yao, T.; Liu, W.; Lin, Y.; Ju, H.; Dong, J.; Zheng, L.; Yan, W.; Zheng, X.; Li, Z.; Wang, X.; Yang, J.; He, D.; Wang, Y.; Deng, Z.; Wu, Y.; Li, Y. Uncoordinated Amine Groups of Metal–Organic Frameworks to Anchor Single Ru Sites as Chemoselective Catalysts toward the Hydrogenation of Quinoline. *J. Am. Chem. Soc.* **2017**, *139*, 9419–9422.

(33) Ye, T.-N.; Li, J.; Kitano, M.; Hosono, H. Unique Nanocages of 12CaO·7Al₂O₃ Boost Heterolytic Hydrogen Activation and Selective Hydrogenation of Heteroarenes over Ruthenium Catalyst. *Green Chem.* **2017**, *19*, 749–756.

(34) Zhang, L.; Wang, X.; Xue, Y.; Zeng, X.; Chen, H.; Li, R.; Wang, S. Cooperation Between the Surface Hydroxyl Groups of Ru–SiO₂@mSiO₂ and Water for Good Catalytic Performance for Hydrogenation of Quinoline. *Catal. Sci. Technol.* **2014**, *4*, 1939–1948.

(35) Chen, F.; Surkus, A.-E.; He, L.; Pohl, M.-M.; Radnik, J.; Topf, C.; Junge, K.; Beller, M. Selective Catalytic Hydrogenation of Heteroarenes with N-Graphene-Modified Cobalt Nanoparticles (Co₃O₄–Co/NGr@α-Al₂O₃). *J. Am. Chem. Soc.* **2015**, *137*, 11718–11724.

(36) Wei, Z.; Chen, Y.; Wang, J.; Su, D.; Tang, M.; Mao, S.; Wang, Y. Cobalt Encapsulated in N-Doped Graphene Layers: An Efficient

and Stable Catalyst for Hydrogenation of Quinoline Compounds. *ACS Catal.* **2016**, *6*, 5816–5822.

(37) Iqbal, S.; Kondrat, S. A.; Jones, D. R.; Schoenmakers, D. C.; Edwards, J. K.; Lu, L.; Yeo, B. R.; Wells, P. P.; Gibson, E. K.; Morgan, D. J.; Kiely, C. J.; Hutchings, G. J. Ruthenium Nanoparticles Supported on Carbon: An Active Catalyst for the Hydrogenation of Lactic Acid to 1,2-Propanediol. *ACS Catal.* **2015**, *5*, 5047–5059.

(38) Kitano, M.; Kanbara, S.; Inoue, Y.; Kuganathan, N.; Sushko, P. V.; Yokoyama, T.; Hara, M.; Hosono, H. Electride Support Boosts Nitrogen Dissociation Over Ruthenium Catalyst and Shifts the Bottleneck in Ammonia Synthesis. *Nat. Commun.* **2015**, *6*, 6731.

(39) Li, W.-Z.; Liu, J.-X.; Gu, J.; Zhou, W.; Yao, S.-Y.; Si, R.; Guo, Y.; Su, H.-Y.; Yan, C.-H.; Li, W.-X.; Zhang, Y.-W.; Ma, D. Chemical Insights into the Design and Development of Face-Centered Cubic Ruthenium Catalysts for Fischer–Tropsch Synthesis. *J. Am. Chem. Soc.* **2017**, *139*, 2267–2276.

(40) Kusada, K.; Kobayashi, H.; Yamamoto, T.; Matsumura, S.; Sumi, N.; Sato, K.; Nagaoka, K.; Kubota, Y.; Kitagawa, H. Discovery of Face-Centered-Cubic Ruthenium Nanoparticles: Facile Size-Controlled Synthesis Using the Chemical Reduction Method. *J. Am. Chem. Soc.* **2013**, *135*, 5493–5496.

(41) Han, S.; Yun, Q.; Tu, S.; Zhu, L.; Cao, W.; Lu, Q. Metallic Ruthenium-Based Nanomaterials for Electrocatalytic and Photocatalytic Hydrogen Evolution. *J. Mater. Chem. A* **2019**, *7*, 24691–24714.

(42) Arrigo, R.; Schuster, M. E.; Xie, Z.; Yi, Y.; Wowsnick, G.; Sun, L. L.; Hermann, K. E.; Friedrich, M.; Kast, P.; Hävecker, M.; Knop-Gericke, A.; Schlögl, R. Nature of the N–Pd Interaction in Nitrogen-Doped Carbon Nanotube Catalysts. *ACS Catal.* **2015**, *5*, 2740–2753.

(43) Wood, K. N.; O’Hayre, R.; Pylypenko, S. Recent Progress on Nitrogen/Carbon Structures Designed for Use in Energy and Sustainability Applications. *Energy Environ. Sci.* **2014**, *7*, 1212–1249.

(44) Xu, X.; Li, Y.; Gong, Y.; Zhang, P.; Li, H.; Wang, Y. Synthesis of Palladium Nanoparticles Supported on Mesoporous N-Doped Carbon and Their Catalytic Ability for Biofuel Upgrade. *J. Am. Chem. Soc.* **2012**, *134*, 16987–16990.

(45) Ouyang, T.; Ye, Y. Q.; Wu, C. Y.; Xiao, K.; Liu, Z. Q. Heterostructures Composed of N-Doped Carbon Nanotubes Encapsulating Cobalt and β-Mo₂C Nanoparticles as Bifunctional Electrodes for Water Splitting. *Angew. Chem., Int. Ed.* **2019**, *58*, 4923–4928.

(46) Yang, H. B.; Hung, S.-F.; Liu, S.; Yuan, K.; Miao, S.; Zhang, L.; Huang, X.; Wang, H.-Y.; Cai, W.; Chen, R.; Gao, J.; Yang, X.; Chen, W.; Huang, Y.; Chen, H. M.; Li, C. M.; Zhang, T.; Liu, B. Atomically Dispersed Ni(I) as the Active Site for Electrochemical CO₂ Reduction. *Nat. Energy* **2018**, *3*, 140–147.

(47) Chen, Y.; Wang, Z.; Mao, S.; Wang, Y. Rational Design of Hydrogenation Catalysts Using Nitrogen-Doped Porous Carbon. *Chin. J. Catal.* **2019**, *40*, 971–979.

(48) Cao, Y.; Mao, S.; Li, M.; Chen, Y.; Wang, Y. Metal/Porous Carbon Composites for Heterogeneous Catalysis: Old Catalysts with Improved Performance Promoted by N-Doping. *ACS Catal.* **2017**, *7*, 8090–8112.

(49) Chandra, D.; Saito, K.; Yui, T.; Yagi, M. Crystallization of Tungsten Trioxide Having Small Mesopores: Highly Efficient Photoanode for Visible-Light-Driven Water Oxidation. *Angew. Chem., Int. Ed.* **2013**, *52*, 12606–12609.

(50) Chandra, D.; Bhaumik, A. Super-Microporous TiO₂ Synthesized by Using New Designed Chelating Structure Directing Agents. *Microporous Mesoporous Mater.* **2008**, *112*, 533–541.

(51) Cui, X.; Surkus, A.-E.; Junge, K.; Topf, C.; Radnik, J.; Kreyenschulte, C.; Beller, M. Highly Selective Hydrogenation of Arenes Using Nanostructured Ruthenium Catalysts Modified With a Carbon–Nitrogen Matrix. *Nat. Commun.* **2016**, *7*, 11326.

(52) Liu, H.; Jiang, T.; Han, B.; Liang, S.; Zhou, Y. Selective Phenol Hydrogenation to Cyclohexanone Over a Dual Supported Pd–Lewis Acid Catalyst. *Science* **2009**, *326*, 1250.

(53) Qadir, K.; Joo, S. H.; Mun, B. S.; Butcher, D. R.; Renzas, J. R.; Aksoy, F.; Liu, Z.; Somorjai, G. A.; Park, J. Y. Intrinsic Relation

between Catalytic Activity of CO Oxidation on Ru Nanoparticles and Ru Oxides Uncovered with Ambient Pressure XPS. *Nano Lett.* **2012**, *12*, 5761–5768.

(54) Ievins, A. D.; Moughton, A. O.; O'Reilly, R. K. Synthesis of Hollow Responsive Functional Nanocages Using a Metal–Ligand Complexation Strategy. *Macromolecules* **2008**, *41*, 3571–3578.

(55) Haul, R.; Gregg, S. J.; Sing, K. S. W. Adsorption, Surface Area and Porosity. *Berichte der Bunsengesellschaft für physikalische Chemie*; Academic Press: London, 1982; Vol. 86; pp 957.

(56) Ohyama, J.; Sato, T.; Yamamoto, Y.; Arai, S.; Satsuma, A. Size Specifically High Activity of Ru Nanoparticles for Hydrogen Oxidation Reaction in Alkaline Electrolyte. *J. Am. Chem. Soc.* **2013**, *135*, 8016–8021.

(57) Lin, L.; Zhu, Q.; Xu, A.-W. Noble-Metal-Free Fe–N/C Catalyst for Highly Efficient Oxygen Reduction Reaction under Both Alkaline and Acidic Conditions. *J. Am. Chem. Soc.* **2014**, *136*, 11027–11033.

(58) Ning, X.; Li, Y.; Dong, B.; Wang, H.; Yu, H.; Peng, F.; Yang, Y. Electron Transfer Dependent Catalysis of Pt on N-Doped Carbon Nanotubes: Effects of Synthesis Method on Metal-Support Interaction. *J. Catal.* **2017**, *348*, 100–109.

(59) Chin, S. Y.; Williams, C. T.; Amiridis, M. D. FTIR Studies of CO Adsorption on Al₂O₃- and SiO₂-Supported Ru Catalysts. *J. Phys. Chem. B* **2006**, *110*, 871–882.

(60) Guglielminotti, E.; Boccuzzi, F.; Manzoli, M.; Pinna, F.; Scarpa, M. Ru/ZrO₂ Catalysts: I. O₂, CO and NO Adsorption and Reactivity. *J. Catal.* **2000**, *192*, 149–157.

(61) The high adsorption energies were noticed if the N-atom of 1a was bonded with the Ru atom with relatively positive charge density (Figure 6a,d). However, less adsorption energies were observed for the cases of N-atom bonded at bridge site (Figure 6b,e) and Ru atom with negative charge density (Figure 6c,f).

(62) Verdinelli, V.; Germán, E.; Luna, C. R.; Marchetti, J. M.; Volpe, M. A.; Juan, A. Theoretical Study of Hydrogen Adsorption on Ru-Decorated (8,0) Single-Walled Carbon Nanotube. *J. Phys. Chem. C* **2014**, *118*, 27672–27680.